

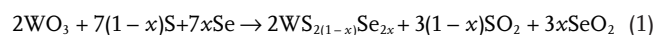
# Synthesis and Enhanced Electrochemical Catalytic Performance of Monolayer $WS_{2(1-x)}Se_{2x}$ with a Tunable Band Gap

Qi Fu, Lei Yang, Wenhui Wang, Ali Han, Jian Huang, Pingwu Du, Zhiyong Fan, Jingyu Zhang, and Bin Xiang\*

Because of their unique structure and impressive physical properties, 2D transition metal dichalcogenides (TMDs) have attracted considerable attention for both fundamental science and device fabrication.<sup>[1–10]</sup> In particular, the indirect-to-direct band gap transformation from the bulk to monolayer form makes monolayer TMDs ideally suited for electronic and optoelectronic device applications.<sup>[11]</sup> For instance, monolayer  $MoS_2$  has attracted considerable interest because of its distinctive electronic, optical, and catalytic properties.<sup>[2,4,12–14]</sup> Band gap engineering is an important strategy to enhance the performance of devices made from monolayer TMDs. A tunable direct band gap would provide great flexibility in the design of such devices with a wide spectrum response. Recently, many efforts have been made to tune the band gap of monolayer  $MoS_2$  by the formation of ternary alloys.<sup>[15–18]</sup> However, band gap modulation for other 2D TMDs still remains challenging. Monolayer  $WS_2$  with a direct band gap of 1.97 eV is another member of the family of TMDs, which also exhibits high potential for optoelectronic device and industry catalysts applications.<sup>[19–22]</sup> Here, we report the first realization of a tunable band gap in monolayer  $WS_{2(1-x)}Se_{2x}$ , which is achieved by varying the Se content. The monolayer configuration was characterized using atomic force microscopy (AFM) and Raman spectroscopy. Atomic-scale analysis was conducted using high-resolution scanning transmission electron microscopy (HRSTEM). The elemental

composition and binding energies were investigated using X-ray photoelectron spectroscopy (XPS). The tunable band gap was confirmed by photoluminescence (PL) spectroscopy. The catalytic activity of the as-synthesized monolayer  $WS_{2(1-x)}Se_{2x}$  was also demonstrated in an electrochemical catalytic reaction for hydrogen evolution.

The synthesis of monolayer  $WS_{2(1-x)}Se_{2x}$  was conducted in a two-temperature zone tube furnace, as shown in Figure 1A (details are given in the Experimental Section and Figure S1, Supporting Information). The schematic illustration in Figure 1B shows the transformation from  $WO_3$  (monoclinic crystal) to  $WS_{2(1-x)}Se_{2x}$  (hexagonal crystal) through simultaneous sulfuration and selenization. The chemical reaction is



The statistical analysis of the effect of different Se contents ( $x = 0.18, 0.3, 0.43$ ) on the triangular domain size is shown in Figure 1C. Representative optical images of monolayer  $WS_{2(1-x)}Se_{2x}$  with different Se contents are presented in the inset. The average domain size of the as-grown monolayer  $WS_{2(1-x)}Se_{2x}$  is  $\approx 26 \mu m$ , indicating that the difference in the Se content exerts a trivial effect on the  $WS_{2(1-x)}Se_{2x}$  domain size growth. Our studies reveal that the carrier gas flow rate plays an important role on monolayer nucleation and growth, determining the size of  $WS_{2(1-x)}Se_{2x}$  triangular domains (Figure S2, Supporting Information). Figure 1D presents an AFM image of the as-grown  $WS_{2(1-x)}Se_{2x}$  ( $x = 0.43$ ). The height profile in the inset shows the 0.92 nm thickness of the monolayer  $WS_{2(1-x)}Se_{2x}$  domain.<sup>[16,23]</sup> Figure 1E presents a scanning electron microscopy (SEM) image of high-density monolayer  $WS_{2(1-x)}Se_{2x}$  ( $x = 0.43$ ) triangular domains with a coverage density of 30%.

Figure 2A presents a scanning transmission electron microscopy (STEM) image of our as-grown monolayer  $WS_{2(1-x)}Se_{2x}$  ( $x = 0.43$ ) with a triangular feature. The indexed selected area electron diffraction pattern is shown in the inset, demonstrating the single-crystal nature of our as-grown monolayer  $WS_{2(1-x)}Se_{2x}$ . HRSTEM was also utilized to characterize the monolayer  $WS_{2(1-x)}Se_{2x}$ , which shows the Z-contrast ( $Z =$  atomic number) as images with atomic-scale resolution, as observed in Figure 2B. We can see the hexagonal rings of the alternative W and S/Se atoms in each unit. For clarity, some of the atoms are denoted by blue and yellow spheres representing W atoms and S/Se atoms, respectively. The homogeneous and brightest spots represent W atoms; the S/Se atoms appear darker than the W atoms because the Z number of W (74) is larger than

Q. Fu, L. Yang, W. Wang, A. Han, J. Huang,  
P. Du, B. Xiang  
Department of Materials Science & Engineering  
CAS Key Lab of Materials for Energy Conversion  
University of Science and Technology of China  
Hefei, Anhui 230026, China  
E-mail: binxiang@ustc.edu.cn



Z. Fan  
Department of Electronic and Computer Engineering  
Hong Kong University of Science and Technology  
Hong Kong SAR 8523, China

J. Zhang  
Molecular Foundry  
Lawrence Berkeley National Laboratory  
1 Cyclotron Rd, Berkeley, CA 94720, USA

B. Xiang  
Synergetic Innovation Center of Quantum  
Information & Quantum Physics  
University of Science and Technology of China  
Hefei, Anhui 230026, China

DOI: 10.1002/adma.201500368

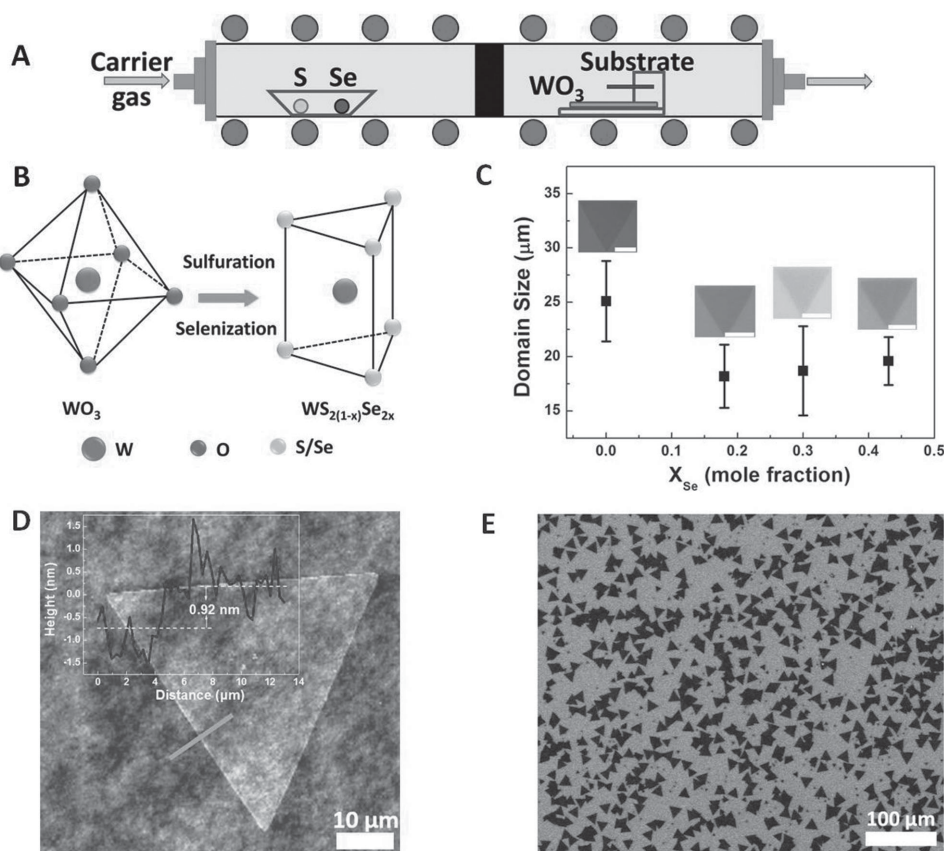


**Figure 1.** A) A schematic illustration of the growth setup. B) A schematic illustration of the transformation from  $\text{WO}_3$  (monoclinic crystal) to  $\text{WS}_{2(1-x)}\text{Se}_{2x}$  (hexagonal crystal) through simultaneous sulfuration and selenization processes. C) Statistical analysis of triangular domain size affected by different Se contents ( $x = 0, 0.18, 0.3, 0.43$ ). Scale bar:  $10 \mu\text{m}$ . D) AFM image of as-grown monolayer  $\text{WS}_{2(1-x)}\text{Se}_{2x}$  ( $x = 0.43$ ). The line profile in the inset indicates the thickness of the as-grown monolayer  $\text{WS}_{2(1-x)}\text{Se}_{2x}$ , triangular domain is  $\approx 0.92 \text{ nm}$ . E) SEM image of high-density monolayer  $\text{WS}_{2(1-x)}\text{Se}_{2x}$  ( $x = 0.43$ ) triangular domains with a coverage density of 30%.

that of S (16) and Se (34). There are three levels of brightness in Figure 2B. The dimmest spots represent the S + S atoms, which are encircled in red; the relatively bright spots are the S + Se atoms, which are encircled in yellow; and the even brighter spots are the Se + Se atoms, which are encircled in blue. The difference in the brightness was further confirmed by a study of three adjacent spots with a brightness line profile as shown in Figure 2C,D. These three spots exhibit an obvious distinction in brightness, representing Se + Se, S + Se, and S + S atoms.<sup>[15]</sup> These results verify the  $\text{WS}_{2(1-x)}\text{Se}_{2x}$  formation of our as-grown monolayer.

Furthermore, the W 4f, S 2p, and Se 3d binding energy in our  $\text{WS}_{2(1-x)}\text{Se}_{2x}$  samples ( $x = 0.18, 0.30, 0.43$ ) was determined using XPS. The XPS measurements were performed with excitation by Al-K $\alpha$  radiation, and the XPS spectra were resolved by multipeak Lorentzian fitting as shown in Figure 2E–G. In Figure 2E, the strong peaks at around 32.9 eV (yellow) and 34.9 eV (green) represent the W 4f<sub>7/2</sub> and W 4f<sub>5/2</sub> binding energy of W<sup>4+</sup>, respectively. The weak peaks at around 35.2 eV (blue) and 38.6 eV (purple) represent the W 4f<sub>7/2</sub> and W 4f<sub>5/2</sub> binding energy of W<sup>6+</sup>, respectively. The peak of W<sup>6+</sup> is mainly due to the existence of adherent  $\text{WO}_3$  on the surface of the substrate.<sup>[24]</sup> The peaks at around 162.6 and 163.8 eV are attributed to S 2p<sub>3/2</sub> and S 2p<sub>1/2</sub> binding energy, respectively, as shown in

Figure 2F. The Se 3d<sub>5/2</sub> and Se 3d<sub>3/2</sub> peaks are located at around 54.9 and 55.8 eV, respectively, as shown in Figure 2G. These results are consistent with previously reported value.<sup>[25,26]</sup>

Raman spectroscopy was also utilized to characterize our as-grown monolayer  $\text{WS}_{2(1-x)}\text{Se}_{2x}$  samples ( $x = 0.18, 0.30, 0.43$ ) as shown in Figure 3A. All the measurements were conducted using a laser with a wavelength of 532 nm (Figure S3, Supporting Information). In the Raman spectra, the positions of the peaks exhibit red shifts with an increase of the Se content. In pure  $\text{WS}_2$ , the strongest peak at  $\approx 350 \text{ cm}^{-1}$  comprises the in-plane vibrational  $E_{2g}^1(\text{M})$  mode, a second-order mode of the longitudinal acoustic phonon 2LA(M) mode, and an in-plane vibrational  $E_{2g}^1(\Gamma)$  mode.<sup>[19,20]</sup> The strong peak at  $\approx 419 \text{ cm}^{-1}$  is attributed to an out-of-plane  $A_{1g}(\Gamma)$  mode.<sup>[19,27,28]</sup> In pure  $\text{WSe}_2$ , the strongest peak at  $\approx 251 \text{ cm}^{-1}$  is attributed to an out-of-plane  $A_{1g}(\Gamma)$  mode and a second-order mode of the longitudinal acoustic phonon 2LA(M) mode (Figure S4, Supporting Information).<sup>[29–31]</sup> With the increase of the Se content in  $\text{WS}_{2(1-x)}\text{Se}_{2x}$ , the peaks at  $\approx 350 \text{ cm}^{-1}$  and  $\approx 419 \text{ cm}^{-1}$  start to exhibit red shifts. This is most likely caused by lattice tensile strain, resulting from the larger radius of Se atom compared to S atom.<sup>[32,33]</sup> The  $A_{1g}(\Gamma)$  mode and 2LA(M) mode peaks of  $\text{WSe}_2$  were clearly observed in  $\text{WS}_{2(1-x)}\text{Se}_{2x}$  ( $x = 0.18, 0.3, 0.43$ ) samples, a notable red shift with the increase of Se content was also observed in

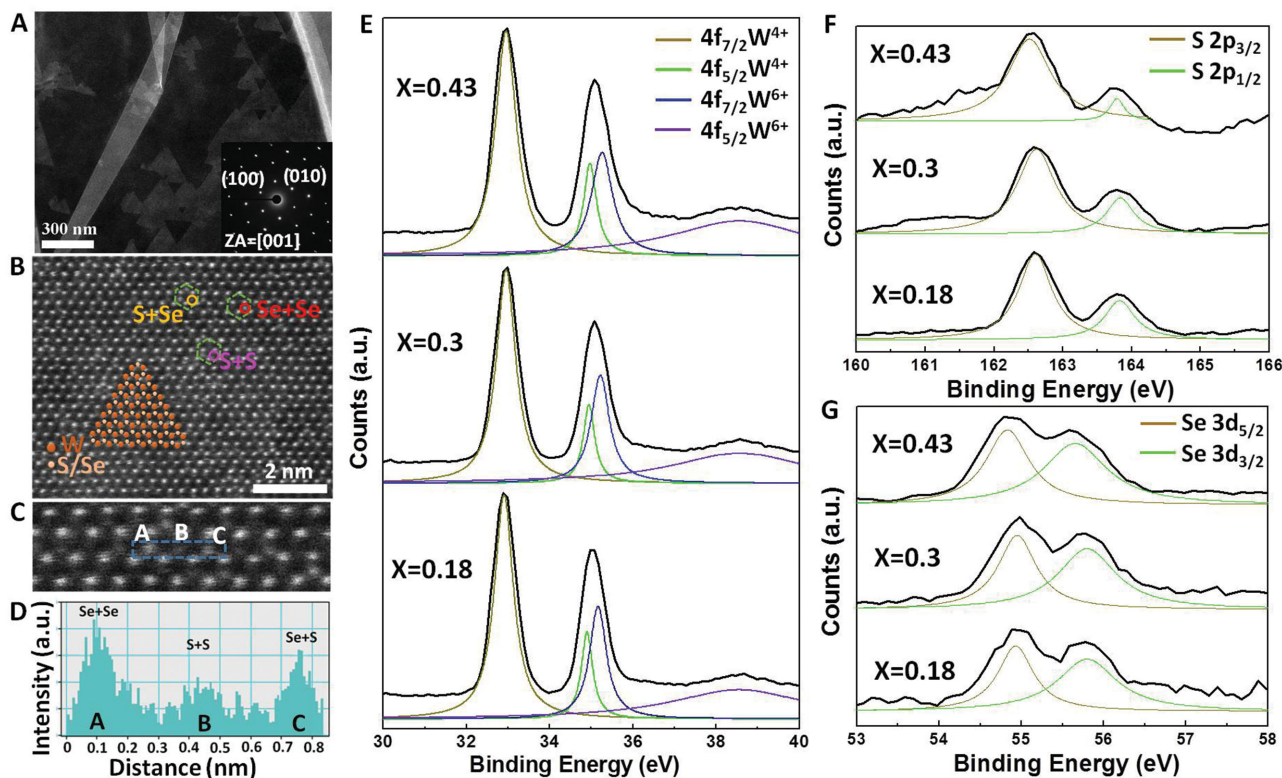


**Figure 2.** A) STEM image of our as-grown monolayer  $WS_{2(1-x)}Se_{2x}$  ( $x = 0.43$ ) triangular domains on a Cu grid. B) HRSTEM image of our as-grown monolayer  $WS_{2(1-x)}Se_{2x}$  ( $x = 0.43$ ). The hexagonal rings consist of alternative W and S/Se atoms as shown in the schematic illustration in the inset. The W atoms are blue and the S/Se atoms are yellow. The spots with different brightness in the three hexagonal rings represent the locations of Se + Se atoms, Se + S atoms, and S + S atoms. C) The discrepancy in the intensity of the three adjacent spots shows the distinguished brightness. D) The intensity profile shows the brightness of the corresponding areas denoted in (C). XPS spectra showing the binding energies of E) W-4f, F) S-2p, and G) Se-3d.

these peaks as shown in Figure 3A. The statistical analysis of the peak positions is shown in Figure 3C. As demonstrated in the HRSTEM image, the substitution between S and Se atoms occurred in a single crystal lattice, which could lead to lattice distortion and thus result in variation of the Raman peak positions. The aggravation of disorder in a molecule induces the broadening of the Raman peaks.<sup>[34,35]</sup>

Figure 3B presents the room-temperature PL spectra of the as-grown monolayer  $WS_{2(1-x)}Se_{2x}$  with different Se contents. Obvious red shift behavior of the PL peaks is also observed upon increasing the Se content. To better understand the tunable band gap behavior, theoretical calculations were also applied to verify the band gap modulation using the generalized gradient approximation of density functional theory (DFT-GGA) method. In pure monolayer  $WS_2$ , a direct band gap of 1.97 eV was observed (PL emission peak at 630 nm), mainly originating from A-exciton emission. This transition represents the direct excitonic transition between the conduction band minimum (CBM) and the valence band maximum (VBM) at the same K point in the Brillouin zone.<sup>[3,22,27]</sup> In monolayer  $WS_2$ , the CBM state mainly consists of the  $d_z^2$  orbital of W cations and the  $p_x$ ,  $p_y$  orbitals of S anions, whereas the VBM state mainly consists of the  $d_{x^2-y^2}$  and  $d_{xy}$  orbitals of W cations and the  $p_x$ ,  $p_y$  orbitals of S anions. The band gap of monolayer  $WS_2$  was determined using the nonbonding  $d$  band structure. For instance, the gap size between the fully occupied  $d_z^2$  orbital of

W cations and the empty  $d_{x^2-y^2}$ ,  $d_{xy}$  orbitals of W cations determines the band gap of the monolayer  $WS_2$ . The interaction between W and S is an important issue for the  $d$  band structure. The bonding mode of W and S is a mixture of ionic bonding and covalent bonding.<sup>[36,37]</sup> As Se atoms replace S atoms, the bonding between W and Se becomes more covalent due to the lower electronegativity value of 2.4 for Se atoms compared with that of 2.5 for S atoms.<sup>[38]</sup> The stronger covalent bonding mode results in the broadening of the fully occupied  $d_z^2$  band. Therefore, a decreased gap size between the fully occupied  $d_z^2$  band and the adjacent empty band is achieved by increasing the Se content.<sup>[37–39]</sup> As a result, in monolayer  $WS_{2(1-x)}Se_{2x}$ , the direct band gap starts to monotonously curtail upon increasing the Se content. The band gap value reaches a minimum at 1.61 eV with a PL emission peak at 772 nm. The band gap variation conforms to our theoretical calculation results (shown in Figure 3D). The band gap of monolayer  $WS_{2(1-x)}Se_{2x}$  can be tuned in a wide range from 1.79 eV to 1.92 eV by adjusting the ratio of S and Se. In addition, the direct band gap configuration is maintained during the modulation in the monolayer  $WS_{2(1-x)}Se_{2x}$ .<sup>[15]</sup> Note that the calculated band gap value is smaller than the value observed in the PL spectra. It is mainly attributed to the use of the standard exchange-correlation functions of the generalized gradient approximation (GGA) in the calculations, which causes the underestimated results for band gap energy.<sup>[40]</sup>

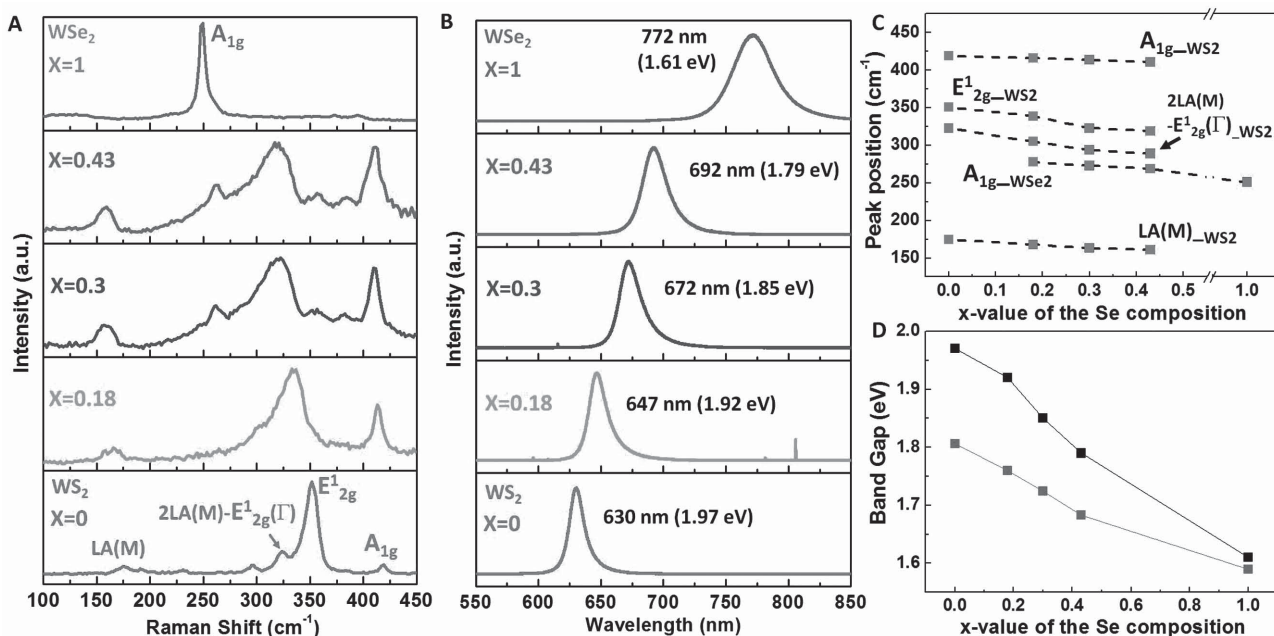


**Figure 3.** A) Raman spectra of the as-grown monolayer  $WS_{2(1-x)}Se_{2x}$  excited by a 532 nm laser. The corresponding chemical content is noted at the top left of each spectrum. B) Room-temperature PL spectra of the as-grown monolayer  $WS_{2(1-x)}Se_{2x}$  excited by a 532 nm laser. The emission peaks position shifts from 630 nm (1.97 eV) to 772 nm (1.61 eV) upon increasing the Se content. C) The statistical analysis of the Raman peak position of the as-grown monolayer  $WS_{2(1-x)}Se_{2x}$ . D) The statistical analysis of the band gap modulation in the as-grown monolayer  $WS_{2(1-x)}Se_{2x}$ . The observed tuning of the band gap in the as-grown monolayer  $WS_{2(1-x)}Se_{2x}$  (black) is consistent with our theoretical calculations (grey).

To evaluate the electrochemical catalytic performance, the as-grown monolayer  $WS_{2(1-x)}Se_{2x}$  was utilized to catalyze a hydrogen evolution reaction (HER) in 0.5 M  $H_2SO_4$ . **Figure 4A** exhibits the schematic diagram of monolayer  $WS_{2(1-x)}Se_{2x}$  triangular utilizing to HER. First, monolayer  $WS_{2(1-x)}Se_{2x}$  triangular domains were transferred from the  $SiO_2/Si$  substrate to a glassy carbon (GC) electrode, which served as the working electrode in a three-electrode system. The reference electrode and the counter electrode were Ag/AgCl electrode (3 M KCl) and Pt wire, respectively (details are given in the Experimental Section). The current density exhibits smaller value by using a graphite rod or GC as the counter electrode (Figure S6, Supporting Information). The polarization curves (Figure 4B) after internal resistance (iR) compensation obtained at a scan rate of  $5 \text{ mV s}^{-1}$  show the normalized current density as a function of the voltage versus RHE in the monolayer  $WS_{2(1-x)}Se_{2x}$  ( $x = 0.43$ ),  $WS_2$ ,  $WSe_2$ , Pt, and bare GC electrode. The cathodic current density determines the quality of the catalytic hydrogen generation reactions.<sup>[12,13,24,41]</sup> Impressively, the monolayer  $WS_{2(1-x)}Se_{2x}$  electrode exhibits the significant HER catalytic activity with a lowest onset overpotential of  $\approx 80 \text{ mV}$  compared to  $WS_2$  (100 mV) and  $WSe_2$  (150 mV). The HER catalytic current density in our monolayer  $WS_{2(1-x)}Se_{2x}$  is ten times higher than in the  $WS_{2(1-x)}Se_{2x}$  nanotubes<sup>[25]</sup> as well as in the  $WS_2$  nanosheets<sup>[42]</sup> at a potential of  $-0.3 \text{ V}$  versus RHE. The large current density at the same potential indicates prominent hydrogen evolution activity and good charge transport from the monolayer  $WS_{2(1-x)}Se_{2x}$  to the supporting GC. The monolayer configuration with a thickness of less than 1 nm causes a highly conductive behavior in the monolayer samples. Particularly, the monolayer surface edge

sites with unsaturated bonds enhance the carrier transportability.<sup>[43]</sup> The electrocatalytic activity was further probed by the measurement of the Tafel plots, as shown in Figure 4C. A smaller Tafel slope suggests a stronger enhancement of the HER rate at a moderate increase of overpotential.<sup>[44,45]</sup> The monolayer  $WS_{2(1-x)}Se_{2x}$  exhibits a lower Tafel slope of  $85 \text{ mV dec}^{-1}$  than that of monolayer  $WSe_2$  ( $100 \text{ mV dec}^{-1}$ ) and  $WS_2$  ( $95 \text{ mV dec}^{-1}$ ). This Tafel slope is smaller than the value of the  $WS_{2(1-x)}Se_{2x}$  nanotubes<sup>[25]</sup> while larger than the Tafel slope of  $60 \text{ mV dec}^{-1}$  reported in the  $WS_2$  nanosheets.<sup>[42]</sup> A non-Ohmic contact between the monolayer and the GC electrode could be responsible for the larger Tafel slope in our samples. The residual polymethyl methacrylate (PMMA) on the surface of the samples after a transfer could result in this non-Ohmic contact. Therefore, the adsorbed molecules have to overcome an extra potential from contact to trigger the reactions for the hydrogen evolution. The stability of the catalytic performance of monolayer  $WS_{2(1-x)}Se_{2x}$  in the HER was also investigated, as shown in Figure 4D. After 1200 cycles (nearly 67 h) in the HER measurement, the activity of  $WS_{2(1-x)}Se_{2x}$  exhibits no significant decay compared with the initial condition, indicating its excellent reliability in the HER. The lowest onset overpotential and largest exchange current density of monolayer  $WS_{2(1-x)}Se_{2x}$  on the GC electrode indicate the great HER activity and potential applications.

In general, the basal plane of monolayer TMD is chemically inert, whereas the edge sites of monolayer TMD are catalytically active.<sup>[45]</sup> However, the basal plane in our as-grown monolayer  $WS_{2(1-x)}Se_{2x}$  could also be chemically active in addition to the exposed triangular domain edges. The introduction of Se into  $WS_2$  crystals induces a slight distortion in the original structure

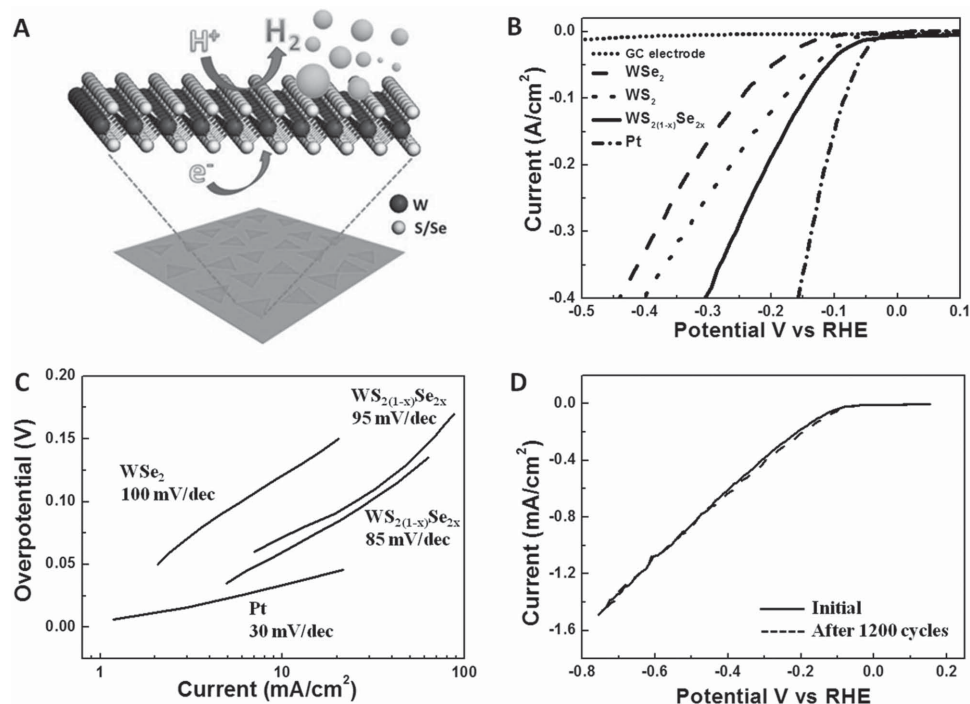


**Figure 4.** A) A schematic illustration of the electrocatalytic activity of monolayer WS<sub>2(1-x)</sub>Se<sub>2x</sub> triangular domains in the HER. B) The polarization curves after iR correction obtained at a voltage sweeping rate of 5 mV s<sup>-1</sup> in the monolayer WS<sub>2(1-x)</sub>Se<sub>2x</sub> ( $x = 0.43$ ), monolayer WS<sub>2</sub>, monolayer WSe<sub>2</sub>, Pt and GC electrode. C) Tafel plots of the WS<sub>2(1-x)</sub>Se<sub>2x</sub> ( $x = 0.43$ ), WS<sub>2</sub>, WSe<sub>2</sub> monolayer, and Pt. D) Stability of the electrocatalytic performance in the monolayer WS<sub>2(1-x)</sub>Se<sub>2x</sub> ( $x = 0.43$ ).

because of the larger radius of Se compared with that of S. This crystal distortion occurs in the basal plane, which could lead to a polarized electric field localized in the basal plane.<sup>[46]</sup> In the presence of an induced electric field, the polarized adsorbed reactants could be easily oriented by this localized electric field, which facilitates the bond breaking of the adsorbed molecules on the basal plane.<sup>[46]</sup> We attribute this effect to the improved HER performance of monolayer WS<sub>2(1-x)</sub>Se<sub>2x</sub> compared with that of monolayer WS<sub>2</sub> and WSe<sub>2</sub>.

In conclusion, we have demonstrated the first synthesis of monolayer WS<sub>2(1-x)</sub>Se<sub>2x</sub> triangular domains on a SiO<sub>2</sub>/Si substrate using a chemical vapor deposition (CVD) method. The configuration and high quality of its crystal structure were confirmed by HRSTEM. The tunable band gap of monolayer WS<sub>2(1-x)</sub>Se<sub>2x</sub> was achieved by varying the ratio of Se and S. The HER catalytic performance of as-grown monolayer WS<sub>2(1-x)</sub>Se<sub>2x</sub> exhibits the lowest overpotential ( $\approx 80$  mV), largest exchange current density, and favorable stability compared with monolayer WS<sub>2</sub> and WSe<sub>2</sub>. These findings broaden our vision of additional electrochemical catalysts and other electronic devices.

## Experimental Section

**Synthesis of Monolayer WS<sub>2(1-x)</sub>Se<sub>2x</sub>:** First, sulfur powder (>99.95%, Sigma Aldrich) and selenium powder (>99.95%, Sigma Aldrich) were placed in zone 1. The selenium powder was placed in a relatively higher temperature region compared with the sulfur powder because of its higher evaporation temperature. The integral molar quantity of S and Se

was preserved at 0.0012 mol, and the ratio of S and Se in the monolayer growth with different  $x$  value was gradually adjusted. The details of S and Se powder weight used in the growth are shown in Table S1 (Supporting Information). Then WO<sub>3</sub> powder (>99.5%, Sigma Aldrich) was uniformly spread on a quartz holder located in zone 2. During all of the monolayer WS<sub>2(1-x)</sub>Se<sub>2x</sub> growth, the loading amount of WO<sub>3</sub> powder was preserved 0.5 g. A silicon substrate coated with a 300-nm-thick SiO<sub>2</sub> layer was placed upside down on the top of the WO<sub>3</sub> with a distance of 5 mm. Before the growth, the substrate was treated with sonication in acetone, isopropyl alcohol (IPA) and deionized (DI) water for 10 min each. The system was vacuumed and then rinsed several times with argon gas mixed with H<sub>2</sub> (5%). First, zone 2 was heated to 830 °C at a rate of 15 °C min<sup>-1</sup>. Then, zone 1 was heated to 300 °C at a rate of 5 °C min<sup>-1</sup>. The two zone temperatures were maintained for 15 min. Finally, the entire system was naturally cooled down to room temperature. The flow of the mixed carrier gas was maintained at a flow rate of 50 sccm during the entire growth process.

**Theoretical Calculation Method:** The band gap of monolayer WS<sub>2(1-x)</sub>Se<sub>2x</sub> was simulated using CASTEP, a package for the density functional theory (DFT) calculation. The ultrasoft pseudopotentials were selected and the Perdew–Burke–Ernzerhof form of generalized gradient approximation (GGA) was used as electron exchange–correlation potential. Plane wave functions were used at a cutoff energy of 500 eV. For geometry optimization, the ions were relaxed until the maximum forces were less than 0.05 eV Å<sup>-1</sup> and the total energy was converged to  $5 \times 10^{-5}$  eV per atom.

**Transfer of As-Grown Monolayer WS<sub>2(1-x)</sub>Se<sub>2x</sub> from Substrate to Carbon Grid and GC Electrode:** Polymethyl methacrylate (PMMA) methylbenzene solution was uniformly spun on a SiO<sub>2</sub>/Si substrate grown with monolayer WS<sub>2(1-x)</sub>Se<sub>2x</sub> triangular domains at a spinning speed of 3000 rpm for 40 s. After being heated at 100 °C for 5 min, the substrate coated with PMMA film was dipped in 5 M KOH solution. Because of its increased affinity to PMMA, the monolayer WS<sub>2(1-x)</sub>Se<sub>2x</sub> triangular domains were detached with the PMMA film from the substrate as

a result of the etching effect by the KOH solution. Then, the isolated PMMA film with  $WS_{2(1-x)}Se_{2x}$  was washed in DI water and overlaid on the carbon grid/GC electrode. The PMMA film was further dissolved by acetone, leaving only monolayer  $WS_{2(1-x)}Se_{2x}$  triangular domains on the carbon grid/GC electrode. A schematic diagram of the transfer process is presented in Figure S5 (Supporting Information).

**Electrocatalytic Characteristics:** All the electrochemical catalytic behavior measurements were conducted in a three-electrode system with an electrochemical analyzer (660E CH Instrument, purchased from Shanghai Chenhua Instrument Co., Ltd.). A bare glass carbon electrode ( $d = 3$  mm) or GC electrode with transferred monolayer  $WS_{2(1-x)}Se_{2x}$  was used as the working electrode. An Ag/AgCl (3 M KCl) electrode was used as the reference electrode and Pt wire was used as the counter electrode. The catalyst solution was 0.5 M  $H_2SO_4$ . The voltage in linear sweep voltammetry was scanned from 0 V to  $-1$  V with a rate of  $5$  mV  $s^{-1}$ . All the potentials were calibrated to a reversible hydrogen electrode (RHE). All the electrocatalytic measurements were performed at room temperature.

## Supporting Information

Supporting Information is available from the Wiley Online Library or from the author.

## Acknowledgements

This work was supported by the National Science Foundation of China (21373196 and 11434009), the National Program for Thousand Young Talents of China, and the Fundamental Research Funds for the Central Universities (WK2060140014 and WK2340000050).

Received: January 23, 2015

Revised: March 29, 2015

Published online: July 8, 2015

- [1] J. Mann, Q. Ma, P. M. Odenthal, M. Isarraraz, D. Le, E. Preciado, D. Barroso, K. Yamaguchi, G. von Son Palacio, A. Nguyen, T. Tran, M. Wurch, A. Nguyen, V. Klee, S. Bobek, D. Sun, T. F. Heinz, T. S. Rahman, R. Kawakami, L. Bartels, *Adv. Mater.* **2014**, *26*, 1399.
- [2] B. Radisavljevic, A. Radenovic, J. Brivio, V. Giacometti, A. Kis, *Nat. Nanotechnol.* **2011**, *6*, 147.
- [3] H. R. Gutierrez, N. Perea-Lopez, A. L. Elias, A. Berkdemir, B. Wang, R. Lv, F. Lopez-Urias, V. H. Crespi, H. Terrones, M. Terrones, *Nano Lett.* **2013**, *13*, 3447.
- [4] A. Splendiani, L. Sun, Y. Zhang, T. Li, J. Kim, C. H. Chim, G. Galli, F. Wang, *Nano Lett.* **2010**, *10*, 1271.
- [5] K. F. Mak, K. He, J. Shan, T. F. Heinz, *Nat. Nanotechnol.* **2012**, *7*, 494.
- [6] T. Cao, G. Wang, W. Han, H. Ye, C. Zhu, J. Shi, Q. Niu, P. Tan, E. Wang, B. Liu, J. Feng, *Nat. Commun.* **2012**, *3*, 887.
- [7] X. Huang, Z. Zeng, H. Zhang, *Chem. Soc. Rev.* **2013**, *42*, 1934.
- [8] K. F. Mak, K. He, C. Lee, G. H. Lee, J. Hone, T. F. Heinz, J. Shan, *Nat. Mater.* **2013**, *12*, 207.
- [9] T. Roy, M. Tosun, J. S. Kang, A. B. Sachid, S. B. Desai, M. Hettick, C. C. Hu, A. Javey, *ACS Nano* **2014**, *8*, 6259.
- [10] R. Lv, J. A. Robinson, R. E. Schaak, D. Sun, Y. Sun, T. E. Mallouk, M. Terrones, *Acc. Chem. Res.* **2014**, *48*, 56.
- [11] W. Zhao, Z. Ghorannevis, L. Chu, M. Toh, C. Kloc, P. Tan, G. Eda, *ACS Nano* **2013**, *7*, 791.
- [12] Y. Li, H. Wang, L. Xie, Y. Liang, G. Hong, H. Dai, *J. Am. Chem. Soc.* **2011**, *133*, 7296.
- [13] M. A. Lukowski, A. S. Daniel, F. Meng, A. Forticaux, L. Li, S. Jin, *J. Am. Chem. Soc.* **2013**, *135*, 10274.
- [14] N. Perea-Lopez, Z. Lin, N. R. Pradhan, A. Iniguez-Rabago, A. L. Elias, A. McCreary, J. Lou, P. M. Ajayan, H. Terrones, L. Balicas, *2D Mater.* **2014**, *1*, 011004.
- [15] Q. Feng, Y. Zhu, J. Hong, M. Zhang, W. Duan, N. Mao, J. Wu, H. Xu, F. Dong, F. Lin, C. Jin, C. Wang, J. Zhang, L. Xie, *Adv. Mater.* **2014**, *26*, 2648.
- [16] Y. Gong, Z. Liu, A. R. Lupini, G. Shi, J. Lin, S. Najmaei, Z. Lin, A. L. Elias, A. Berdemir, G. You, H. Terrones, M. Terrones, R. Vajtai, S. T. Pantelides, S. J. Pennycook, J. Lou, W. Zhou, P. M. Ajayan, *Nano Lett.* **2014**, *14*, 442.
- [17] M. Zhang, J. Wu, Y. Zhu, D. O. Dumcenco, J. Hong, N. Mao, S. Deng, Y. Chen, Y. Yang, C. Jin, S. H. Chaki, Y. Huang, J. Zhang, L. Xie, *ACS Nano* **2014**, *8*, 7130.
- [18] Z. Lin, M. T. Thee, A. L. Elias, S. Feng, C. Zhou, K. Fujisawa, N. Perea-Lopez, V. Carozo, H. Terrones, M. Terrones, *APL Mater.* **2014**, *2*, 092514.
- [19] C. Cong, J. Shang, X. Wu, B. Cao, N. Peimyoo, C. Qiu, L. Sun, T. Yu, *Adv. Opt. Mater.* **2014**, *2*, 131.
- [20] A. Berkdemir, H. R. Gutierrez, A. R. Botello-Mendez, Nestor Perea-Lopez, A. L. Elias, C.-I. Chia, B. Wang, V. H. Crespi, F. Lopez-Urias, J.-C. Charlier, H. Terrones, M. Terrones, *Sci. Rep.* **2013**, *3*, 1755.
- [21] J. Bonde, P. G. Moses, T. F. Jaramillo, J. K. Nørskov, I. Chorkendorff, *Faraday Discuss.* **2008**, *140*, 219.
- [22] N. Perea-Lopez, A. L. Elias, A. Berkdemir, A. Castro-Beltran, H. R. Gutierrez, S. Feng, R. Lv, T. Hayashi, F. Lopez-Urias, S. Ghosh, B. Muchharla, S. Talapatra, H. Terrones, M. Terrones, *Adv. Funct. Mater.* **2013**, *23*, 5511.
- [23] Y. Zhang, Y. Zhang, Q. Ji, J. Ju, H. Yuan, J. Shi, T. Gao, D. Ma, M. Liu, Y. Chen, X. Song, H. Y. Hwang, Y. Cui, Z. Liu, *ACS Nano* **2013**, *7*, 8963.
- [24] A. Avsar, J. Y. Tan, T. Taychatanapat, J. Balakrishnan, G. K. W. Koon, Y. Yeo, J. Lahiri, A. Carvalho, A. S. Rodin, E. C. T. Ofarrell, G. Eda, A. H. Castro Neto, B. Ozyilmaz, *Nat. Commun.* **2014**, *5*, 4875.
- [25] K. Xu, F. Wang, Z. Wang, X. Zhan, Q. Wang, Z. Cheng, M. Safdar, J. He, *ACS Nano* **2014**, *8*, 8468.
- [26] A. Chernikov, T. C. Berkelbach, H. M. Hill, A. Rigosi, Y. Li, O. B. Aslan, D. R. Reichman, M. S. Hybertsen, T. F. Heinz, *Phys. Rev. Lett.* **2014**, *113*, 076802.
- [27] A. L. Elias, N. Perea-Lopez, A. Castro-Beltran, A. Berkdemir, R. Lv, S. Feng, A. D. Long, T. Hayashi, Y. A. Kim, M. Endo, H. R. Gutierrez, N. R. Pradhan, L. Balicas, T. E. Mallouk, F. Lopez-Urias, H. Terrones, M. Terrones, *ACS Nano* **2013**, *7*, 5235.
- [28] H. Terrones, E. Del Corro, S. Feng, J. M. Poumirol, D. Rhodes, D. Smirnov, N. R. Pradhan, Z. Lin, M. Nguyen, A. L. Elias, T. Mallouk, L. Balicas, M. Pimenta, M. Terrones, *Sci. Rep.* **2014**, *4*, 4215.
- [29] H. Sahin, S. Tongay, S. Horzum, W. Fan, J. Zhou, J. Li, J. Wu, F. M. Peeters, *Phys. Rev. B* **2013**, *87*, 165409.
- [30] H. Wang, D. Kong, P. Johanes, J. J. Cha, G. Zheng, K. Yan, N. Liu, Y. Cui, *Nano Lett.* **2013**, *13*, 3426.
- [31] E. Corro, H. Terrones, A. Elias, C. Fantini, S. Feng, M. Nguyen, T. Mallouk, M. Terrones, M. A. Pimenta, *ACS Nano* **2014**, *8*, 9629.
- [32] C. Rice, R. J. Young, R. Zan, U. Bangert, *Phys. Rev. B* **2013**, *87*, 081307.
- [33] A. Castellanos-Gomez, R. Roldan, E. Cappelluti, M. Buscema, F. Guinea, H. S. J. van der Zant, G. A. Steele, *Nano Lett.* **2013**, *13*, 5361.
- [34] K. Nakamura, M. Fujitsuka, M. Kitajima, *Phys. Rev. B* **1990**, *41*, 12260.
- [35] G. Gouadec, P. Colombari, *Prog. Cryst. Growth Charact. Mater.* **2007**, *53*, 1.

- [36] A. D. Yoffe, *Chem. Soc. Rev.* **1976**, 5, 51.
- [37] M. Chhowalla, H. S. Shin, G. Eda, L. J. Li, K. P. Loh, H. Zhang, *Nat. Chem.* **2013**, 5, 263.
- [38] W. Gordy, W. J. O. Thomas, *J. Chem. Phys.* **1956**, 24, 439.
- [39] H. J. Conley, B. Wang, J. I. Ziegler, R. F. Haglund Jr., S. T. Pantelides, K. I. Bolotin, *Nano Lett.* **2013**, 13, 3626.
- [40] S. Lebègue, O. Eriksson, *Phys. Rev. B* **2009**, 79, 115409.
- [41] M. A. Lukowski, A. S. Daniel, C. R. English, F. Meng, A. Forticaux, R. J. Hamers, S. Jin, *Energy Environ. Sci.* **2014**, 7, 2608.
- [42] D. Voiry, H. Yamaguchi, J. Li, R. Silva, D. Alves, T. Fujita, M. Chen, T. Asefa, V. Shenoy, G. Eda, M. Chhowalla, *Nat. Mater.* **2013**, 12, 850.
- [43] B. Hinnemann, P. G. Moses, J. Bonde, K. P. Jørgensen, J. H. Nielsen, S. Horch, I. Chorkendorff, J. K. Nørskov, *J. Am. Chem. Soc.* **2005**, 127, 5308.
- [44] D. Merki, X. Hu, *Energy Environ. Sci.* **2011**, 4, 3878.
- [45] J. Shi, D. Ma, G. Han, Y. Zhang, W. Ji, T. Gao, J. Sun, X. Song, C. Li, Y. Zhang, X. Lang, Y. Zhang, Z. Liu, *ACS Nano* **2014**, 8, 10196.
- [46] G. A. Somorjai, *Topics Catal.* **2002**, 18, 158.
-